

Sinogram-consistency learning in CT for metal artifact reduction

Hyung Suk Park*, Yong Eun Chung†, Sung Min Lee‡, Hwa Pyung Kim‡, and Jin Keun Seo‡

* Division of Strategic Research, National Institute for Mathematical Sciences, Daejeon, 34047, South Korea

† Department of Radiology, Yonsei University College of Medicine, Seoul, 03722, South Korea

‡ Department of Computational Science and Engineering, Yonsei University, Seoul, 03722, South Korea

Abstract—This paper proposes a sinogram consistency learning method to deal with beam-hardening related artifacts in polychromatic computerized tomography (CT). The presence of highly attenuating materials in the scan field causes an inconsistent sinogram, that does not match the range space of the Radon transform. When the mismatched data are entered into the range space during CT reconstruction, streaking and shading artifacts are generated owing to the inherent nature of the inverse Radon transform. The proposed learning method aims to repair inconsistent sinograms by removing the primary metal-induced beam-hardening factors along the metal trace in the sinogram. Taking account of the fundamental difficulty in obtaining sufficient training data in a medical environment, the learning method is designed to use simulated training data. We use a patient-type specific learning model to simplify the learning process. The quality of sinogram repair was established through data inconsistency-evaluation and acceptance checking, which were conducted using a specially designed inconsistency-evaluation function that identifies the degree and structure of mismatch in terms of projection angles. The results show that our method successfully corrects sinogram inconsistency by extracting beam-hardening sources by means of deep learning.

Index Terms—Tomographic image reconstruction, Computerized tomography, Metal artifact reduction, Deep learning.

I. INTRODUCTION

In computerized tomography (CT), the presence of highly attenuating materials such as metal, concentrated iodinated contrast media or bone complicates reconstruction [1], [5], by violating an assumption of the forward model: that sinogram data are the Radon transform of an image. The increasing use of metallic implants in a generally aging population makes metal-induced artifacts a major impediment to CT diagnosis. In addition, the widely favored low-dose CT protocols that require reduction of tube voltage and/or tube current tend to accentuate artifacts related to these highly attenuating materials, because decreased X-ray tube voltage or current causes more-severe beam hardening, scattering, photon starvation, and photon noise [3], [8]. The mismatched projection data due to these effects cause severe streaking and shading artifacts in the reconstructed CT images. Although extensive research efforts have sought to improve CT reconstruction methods, tackling metal-related artifacts is a very challenging problem because the inconsistent data induced by metal depend nonlinearly on the geometries and placements of the metal objects.

Manuscript received XXX; revised XXX. Corresponding author: J. K. Seo (email: seoj@yonsei.ac.kr).

This paper uses a deep learning approach to repair sinogram inconsistencies, so as to minimize artifacts induced by highly attenuating material. The proposed learning method aims to correct only the main sources of beam-hardening artifacts, while leaving fine data structures intact. The various complicated metaltissue interactions are ignored because it is very difficult to collect training data (i.e., pairs of artifact-free and artifact-contaminated CT images) from patients. We use simulated training data and phantom experimental data (not medical data) to correct the primary beam-hardening factor of metals along a sinusoidal metal trace. The beam-hardening factors due to metals are expected to lie on a very-low-dimensional manifold, thus allowing easy extraction of beam-hardening features in a supervised way. We employ a U-net for learning the nonlinear beam-hardening features. This neural network, trained by non-medical training data, is applied to medical CT data for metal artifact reduction (MAR).

We also develop a method to assess the quality of the input (measured sinogram data) and output (the repaired sinogram) of deep learning. It uses the integral of the projection data as a function of the projection angle, which changes in response to inconsistencies along the trace of highly attenuating materials. The variations in the pattern over the projection angle contain information regarding the artifacts: i.e., low- and high-frequency components are related to shading and streaking artifacts, respectively. Given these observations, it evaluates the standard deviation of each component to assess the streaking and shading artifacts separately, by quantitatively evaluating the data defects induced by highly attenuating materials.

To be precise, let $\mathbf{x}(\varphi, s)$ (input data for deep learning) represent the projection data at projection angle $\varphi \in [0, 2\pi]$ and detector position $s \in \mathbb{R}$. For simplicity, we shall restrict to considering two-dimensional parallel-beam CT. According to the Lambert-Beer's law [12], [13], the CT sinogram data \mathbf{x} can be expressed as

$$\mathbf{x}(\varphi, s) = -\ln \left(\int \eta(E) \exp \left\{ -[\mathcal{R}(\mu_E)](\varphi, s) \right\} d_E \right), \quad (1)$$

where μ_E denotes the attenuation coefficient distribution at photon energy level E , $\eta(E)$ represents fractional energy at E [7], [10], and $\mathcal{R}(\mu_E)$ is the Radon transform of μ_E . See Fig. 1. Let Y denote the range space of the Radon transform \mathcal{R} . Then, Y can be viewed as a subspace of the sinogram space X .

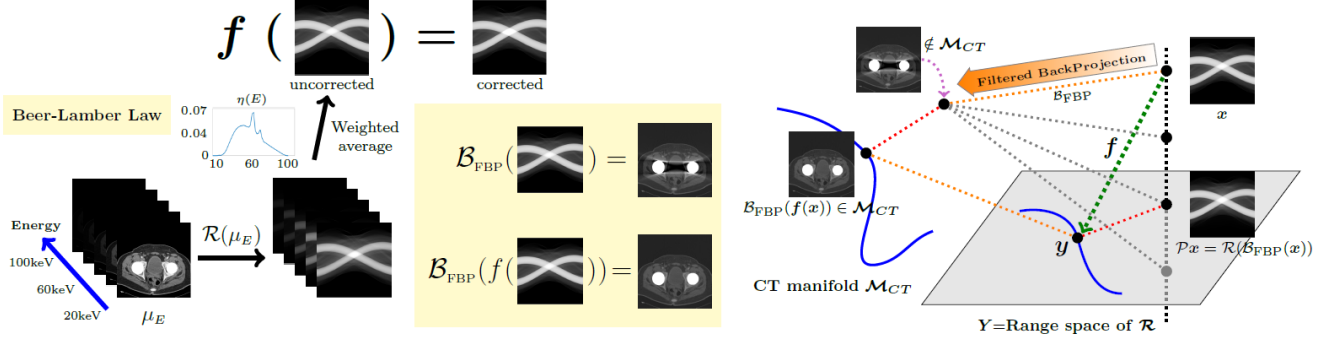


Fig. 1. Schematic diagram of data inconsistency correction in polychromatic X-ray CT. (Left bottom) Images of μ_E over $20\text{keV} \leq E \leq 120\text{ keV}$ and the corresponding Randon transforms. (Left) The sinogram data is approximately a weighted sum of the Radon transforms. Data inconsistencies are caused by the energy-dependent behavior of the attenuation distribution. (Middle-bottom) Filtered backprojections \mathcal{B}_{FBP} of the uncorrected \mathbf{x} and corrected data $f(\mathbf{x})$. (Right) Inconsistency artifact is related to the degree of discrepancy between \mathbf{x} and the range space Y of Radon transform. We need to extract the source of artifacts in the data \mathbf{x} by learning the features considering CT image information (i.e. CT manifold \mathcal{M}_{CT}).

The goal is to learn the sinogram correction function $f : X \rightarrow Y$ such that $\mathcal{B}_{\text{FBP}}(f(\mathbf{x}))$ is artifact-removed image, where \mathcal{B}_{FBP} represents the filtered backprojection (FBP) operator. Noting that the orthogonal projection of \mathbf{x} onto Y is $\mathcal{P}\mathbf{x} = \mathcal{R}(\mathcal{B}_{\text{FBP}}(\mathbf{x}))$, we have $\mathcal{B}_{\text{FBP}}(\mathbf{x}) = \mathcal{B}_{\text{FBP}}(\mathcal{P}\mathbf{x})$. Clearly, $f = \mathcal{R}\mathcal{B}_{\text{FBP}}$ is not appropriate for MAR. Numerous experiments indicate that the degree of metal-associated artifacts is linked to $\mathbf{x} - \mathcal{P}\mathbf{x}$. Roughly speaking, the L^2 -norm of the difference $f(\mathbf{x}) - \mathcal{P}\mathbf{x}$ seems to be comparable to that of $\mathbf{x} - \mathcal{P}\mathbf{x}$. Various numerical experiments show that the proposed deep learning method provides the proper correction of the inconsistent sinogram with preserving its fine-structure. To confirm the goodness of the sinogram repair, we use the above-mentioned indicator for automatic evaluation of the output $f(\mathbf{x})$.

The results suggest that the proposed deep learning method using simulated training data can appropriately correct an inconsistent sinogram for MAR. The proposed method of acceptance checking the output also works well, and it compensates for the drawback of deep learning being an empirical method (and thus not rigorous).

II. METHOD

A. Learning objectives and U-net

Let $\mathbf{x} \in X$ represent a sinogram data in two-dimensional parallel-beam CT, where $X = L^2([0, 2\pi) \times \mathbb{R})$ is the space of square integrable functions with its norm $\|\mathbf{x}\| = \sqrt{\int_0^{2\pi} \int_{\mathbb{R}} |\mathbf{x}(\varphi, s)|^2 ds d\varphi}$. Let Y be the range space of Radon transform \mathcal{R} , a subspace of X . To avoid notational complexity and for ease of explanation, we use the same notations $(\mathbf{x}, \mathbf{y}, X, Y)$ to represent their discrete versions, used in the practice.

In the presence of the high attenuation materials such as metallic objects, \mathbf{x} may not fit with Y and the inconsistency of \mathbf{x} can be quantified by

$$d_{\mathbf{x}} := \min_{\mu \in L^2(\mathbb{R}^2)} \|\mathcal{R}(\mu) - \mathbf{x}\|. \quad (2)$$

The mismatch $d_{\mathbf{x}}$ is somehow related to the degree of artifacts in the image reconstructed by the filtered back projection

(FBP) method. Denoting FBP operator by \mathcal{B}_{FBP} , the reconstructed image $\mathcal{B}_{\text{FBP}}(\mathbf{x})$ can be viewed as the least-square fitting solution, in the sense that

$$\mathcal{B}_{\text{FBP}}(\mathbf{x}) := \underset{\mu \in L^2(\mathbb{R}^2)}{\text{argmin}} \|\mathcal{R}(\mu) - \mathbf{x}\| \quad (3)$$

where ‘argmin’ stands for the argument of the minimum. Hence, the projection operator from X onto Y is expressed as $\mathcal{P} = \mathcal{R}\mathcal{B}_{\text{FBP}}$.

The goal is to find a suitable correction map $f : \mathbf{x} \mapsto \mathbf{y}$ for metal artifact reduction in such a way that $\mathbf{y} \approx \mathcal{R}(\mu_{E_*})$ with μ_{E_*} being the attenuation distribution at a fixed energy E_* . Imagine that \mathcal{M}_{CT} is a manifold \mathcal{M} on which various monochromatic CT images are residing. The manifold \mathcal{M}_{CT} should not include images having serious metal artifacts, as shown in Fig. 1.

The map f must take account of this CT manifold \mathcal{M}_{CT} , because \mathcal{M}_{CT} is regarded as prior information of CT images. Hence, $f(\mathbf{x})$ should be determined by not only \mathbf{x} but also the manifold \mathcal{M}_{CT} . Due to highly nonlinear and complicated structure of \mathcal{M}_{CT} , it could be very difficult to find f without using machine learning techniques.

We adopt U-net to learn f . Denoting f_{ed} the feed forward map corresponding to f , the relation between an input vector \mathbf{x} and an output vector is expressed as

$$\mathbf{y} = f(\mathbf{x}) = f_{\text{ed}}(\mathbf{x}; \mathbf{w}_1, \dots, \mathbf{w}_L) \quad (4)$$

where \mathbf{w}_l is the vector including the weight and bias for l^{th} layer. We collect a set of training data $\{(\mathbf{x}^{(i)}, \mathbf{y}^{(i)})\}_{i=1}^N$ and determine the vectors $\mathbf{w}_1, \dots, \mathbf{w}_L$ by solving

$$\underset{(\mathbf{w}_1, \dots, \mathbf{w}_L)}{\text{argmin}} \frac{1}{N} \sum_{i=1}^N \|f_{\text{ed}}(\mathbf{x}^{(i)}; \mathbf{w}_1, \dots, \mathbf{w}_L) - \mathbf{y}^{(i)}\|^2 \quad (5)$$

The most fundamental challenge is to collect enough medical image data to be well-labeled $\{(\mathbf{x}^{(i)}, \mathbf{y}^{(i)})\}$. This problem seems to be very difficult to solve. To address this fundamental disadvantages, we develop a patient-type specific learning method, which simplify the way for learning f from a simulated or ex-vivo training set. The proposed method fixes

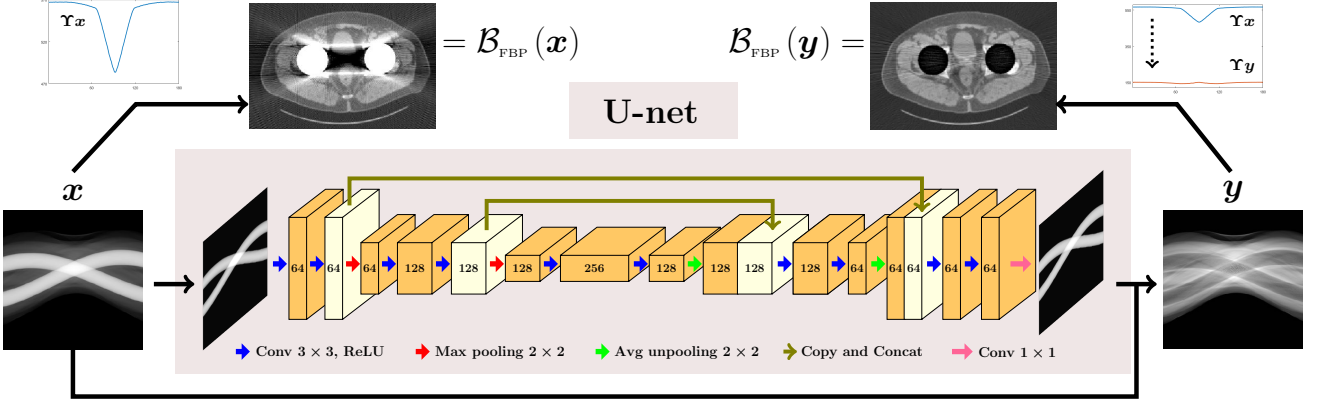


Fig. 2. Deep learning architecture relying on operations of segmentation, convolutional and pooling layers, and rectified linear units (ReLU). To address the difficulties of collecting training data in a CT clinical environment, we use a patient-type specific learning model (e.g. hip replacements) and simplify the learning process.

only major beam-hardening sources along the metal trace and does not touch relatively minor artifact sources. Noting that the nonlinear beam-hardening factor is determined mainly by the geometry and the arrangement of the metal objects, it is possible to learn the sinogram correction from simulated or ex-vivo data. Fig. 2 depicts a rough schematic of this approach. A more detailed explanation is given in section III.

B. Inconsistent indicator

This section provides a method for quantitative evaluation of artifacts from sinogram data \mathbf{x} . It can be used to access whether the correction $f(\mathbf{x})$ is acceptable. Define

$$\Upsilon\mathbf{x}(\varphi) := \int_{\mathbb{R}} \mathbf{x}(\varphi, s) ds \quad (6)$$

This $\Upsilon\mathbf{x}$ can be divided into its low frequency part $\Upsilon\mathbf{x}_L$ and its high frequency part $\Upsilon\mathbf{x}_H$:

$$\Upsilon\mathbf{x}(\varphi) = \Upsilon\mathbf{x}_L(\varphi) + \Upsilon\mathbf{x}_H(\varphi), \quad \varphi \in (0, 2\pi]. \quad (7)$$

Note that $\frac{d}{d\varphi}\Upsilon\mathbf{x}(\varphi) = 0$ for all $\varphi \in [0, 2\pi]$ when the residual $\mathbf{x} - \mathcal{P}\mathbf{x}$ is zero. Hence, the standard deviation of $\Upsilon\mathbf{x}$, denoted by $\text{std}(\Upsilon\mathbf{x})$, quantifies the amount of variation of the inconsistency. The crucial observations are the followings:

- High frequency mismatch $\text{std}(\Upsilon\mathbf{x}_H)$ (associated with abrupt change of $\Upsilon\mathbf{x}$) causes bright and dark streaking artifacts in the CT image.
- Low frequency mismatch $\text{std}(\Upsilon\mathbf{x}_L)$ (associated with a smoothly varying part of $\Upsilon\mathbf{x}$ with respect to φ) generates shading artifacts in the CT image.

Based on the above observation, we propose a mismatch metric:

$$d_{\alpha}^{\text{MA}}(\mathbf{x}) = \text{std}(\Upsilon\mathbf{x}_L)(1 + \alpha \text{std}(\Upsilon\mathbf{x}_H)), \quad (8)$$

where α is the weighting parameter. This $d_{\alpha}^{\text{MA}}(\mathbf{x})$ is somehow related to the quantity of $\|\frac{d}{d\varphi}\Upsilon\mathbf{x}_L\|_{L^2((0, 2\pi])}(1 + \alpha \|\frac{d}{d\varphi}\Upsilon\mathbf{x}_L\|_{L^2((0, 2\pi])})$. Fig. 3 illustrates the behavior of $\Upsilon\mathbf{x}(\varphi)$ and $\frac{d^2}{d\varphi^2}\Upsilon\mathbf{x}(\varphi)$ using numerical phantom containing two disk-shaped metallic objects (titanium) occupying the

region D_1 and D_2 . In this simulation, we only consider the beam hardening artifacts for simplicity. The \mathbf{x} is consistent in all the regions except the diamond shaped area $A_{\diamond} := \{(\varphi, s) : \mathcal{R}\chi_{D_1}(\varphi, s)\mathcal{R}\chi_{D_2}(\varphi, s) \neq 0\}$, where χ_D is the characteristic function, that is, $\chi_D = 1$ on D and zero otherwise. This local inconsistency of \mathbf{x} on A_{\diamond} corresponds to variation of $\Upsilon\mathbf{x}$ on the interval $A_{\diamond,1} := \{\varphi : (\varphi, s) \in A_{\diamond}\}$. The image μ_{CT} in the most left image in Fig. 3 can be reconstructed by the filtered backprojection (FBP) formula [2]. Note that μ_{CT} is the solution of the minimization problem in (5).

From the inherent nature of the least squares approach (5), the local inconsistency of \mathbf{x} on A_{\diamond} generates severe global artifacts in μ_{CT} , which appear as streaking and shading artifacts. As illustrated in Fig. 3, the abrupt changes in $\Upsilon\mathbf{x}(\varphi)$ between projection views occur at $\varphi = \pi/2$ and $\varphi \approx 7\pi/18, 11\pi/18$. These abrupt discrepancies are mapped to the bright and dark streaking artifacts between the boundaries of two metallic objects in the μ_{CT} . Moreover, the gradually varying inconsistency in the $A_{\diamond,1} = [7\pi/18, 11\pi/18]$ interval causes shading artifacts between or near the two metallic objects.

The proposed acceptance-check method is simply comprised of three main steps.

- 1) In the first step, $\Upsilon\mathbf{x}$ for the measured projection data \mathbf{x} is calculated.
- 2) Then, the low-pass filtered component of $\Upsilon\mathbf{x}$, i.e., $\Upsilon\mathbf{x}_L$ is computed based on the penalized least squares method [6], and $\Upsilon\mathbf{x}_H = \Upsilon\mathbf{x} - \Upsilon\mathbf{x}_L$ is obtained.
- 3) Finally, the d_{α}^{MA} in (8) is calculated by computing the standard deviations of $\Upsilon\mathbf{x}_L$ and $\Upsilon\mathbf{x}_H$.

As shown in Fig. 4 (first row), the smoothly varying change of $\Upsilon\mathbf{x}$ primarily encapsulated within $\Upsilon\mathbf{x}_L$, whereas abrupt change of $\Upsilon\mathbf{x}$ is primarily contained within $\Upsilon\mathbf{x}_H$.

Next, we consider \mathbf{x} with additive Poisson noise. In that case, the photon noise distributed over the entire projection domain causes the mismatch of \mathbf{x} and can be expressed as an abrupt change in corresponding $\Upsilon\mathbf{x}$. The μ_{CT} is corrupted by the noise-induced streaking artifacts. Second row in Fig. 4 illustrates the behavior of $\Upsilon\mathbf{x}$, $\Upsilon\mathbf{x}_L$, and $\Upsilon\mathbf{x}_H$ under additive Poisson noise for the phantom used in Fig. 3. The abrupt

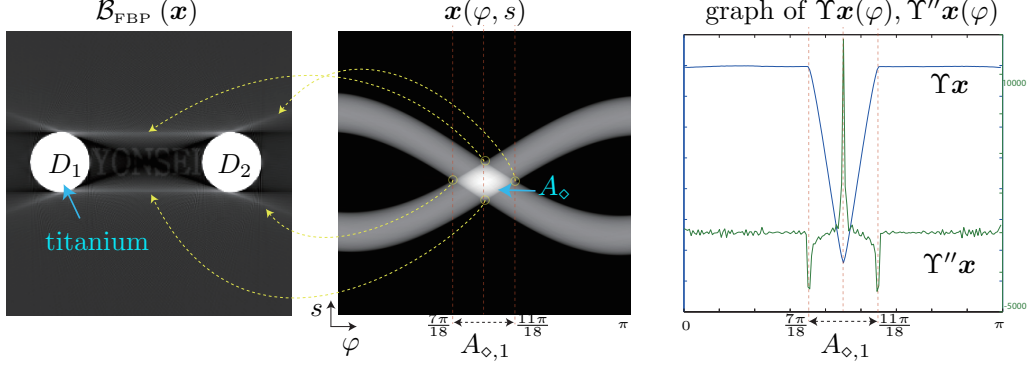


Fig. 3. Left figure shows the CT image μ_{CT} for numerical phantom containing two disk-shaped metallic objects (titanium) occupying the region D_1 and D_2 . The attenuation coefficient of background image (marked by “YONSEI”) is assumed to be the constant with energy E . Middle and right figures show projection data \mathbf{x} and graph of $\Upsilon\mathbf{x}(\varphi)$ and $\frac{d^2}{d\varphi^2}\Upsilon\mathbf{x}(\varphi)$ of the phantom in the left figure, respectively. Here, CT image is simulated at energy range between 0-100 keV ($C=250$ HU/W=2500 HU).

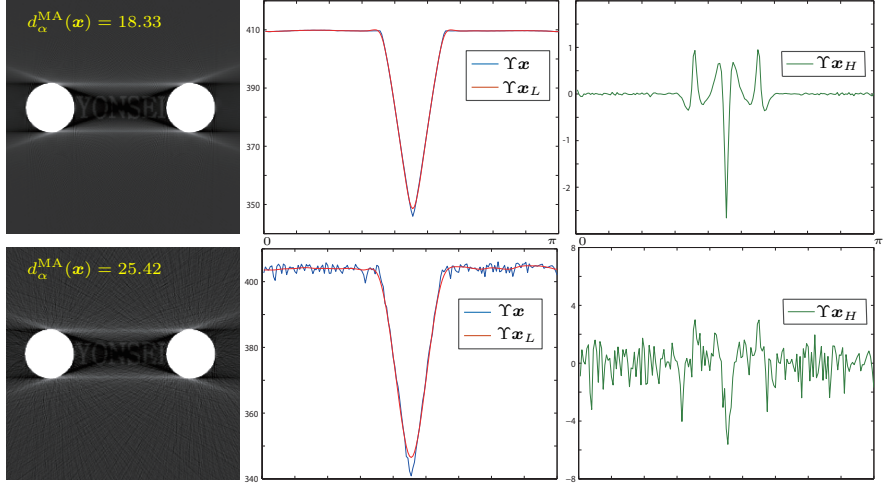


Fig. 4. Illustration of the behavior of $\Upsilon\mathbf{x}$, $\Upsilon\mathbf{x}_L$, and $\Upsilon\mathbf{x}_H$ for the phantom used in Fig. 3 without (first low) and with additive noise (second low). Here, $d_\alpha^{MA}(\mathbf{x})$ in (8) is computed with $\alpha = 0.5$. ($C=250$ HU/W=2500 HU for CT image).

change in $\Upsilon\mathbf{x}_H$ over the entire interval of $[0, \pi]$ is primarily due to the Poisson noise (as well as beam hardening), which yields additional streaking artifacts compared to the noise-free phantom result shown in Fig. 3. The metric d_α^{MA} in (8) can quantify the extent of inconsistency that generates the streaking artifacts.

III. RESULTS

The proposed network consists of a contracting path and an expansive path (see Fig. 2). The contracting path contains convolutions with a size of 3×3 , each followed by a rectified linear unit (ReLU), along with 2×2 max pooling for down-sampling. The expansive path used 2×2 average unpooling instead of max pooling for upsampling. It was concatenated with the correspondingly cropped feature from the contracting path. At the last layer a 1×1 convolution is used to reduce the dimensions. To train the network, we used 3780 CT sinogram data with a size of 368×180 for two metallic objects (iron) by

changing their shape and placement. The cost function (5) was minimized using the RMSPropOptimizer [14] with a learning rate of 0.001, weight decay of 0.9, and mini-batch size of 32 at each epoch. The number of epoch was 2000. Training was implemented by Tensorflow [15] on a CPU (Intel(R) Core(TM) i7-6850K, 3.60GHz) and four GPU (NVIDIA GTX-1080, 8GB) system. The network required approximately 1 day for training.

We performed the proposed method using numerical simulation. In our simulations, projection data \mathbf{x} was generated using attenuation coefficient given in [9] with an X-ray tube voltage of 100kVp [4] with Poisson noise. Other causes of metal artifacts, such as scattering and nonlinear partial volume effects were not considered. Because the proposed learning method only correct the main beam-hardening source along the metal trace, the method needs to apply exclusively on metal trace. We trained to generate metal-induced inconsistent data from metal trace with only thickness information of metal.

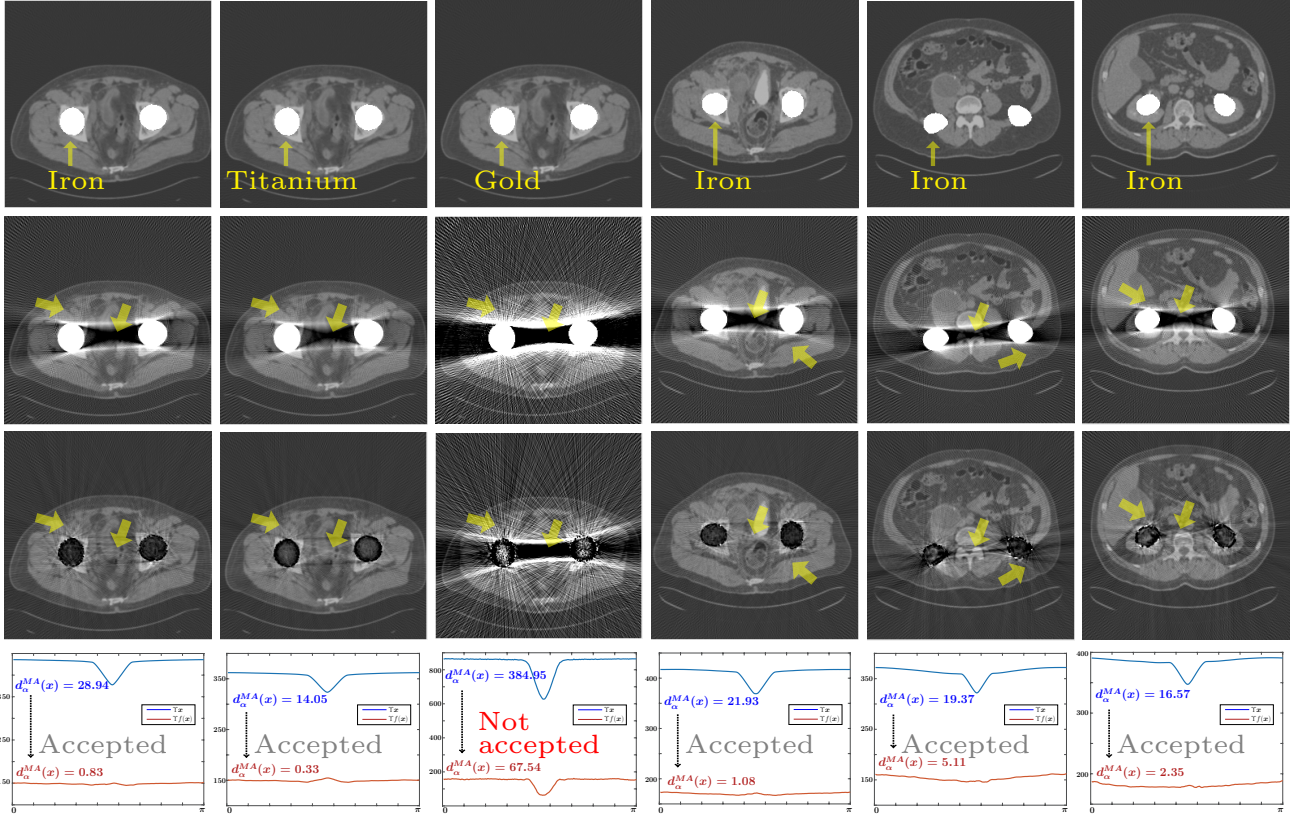


Fig. 5. Example images showing MAR results by sinogram-consistency learning for variations of metal geometries and different metals with different tissue backgrounds. The first, second, third and fourth rows show the reference, uncorrected image, corrected image and the plot of Υ , respectively. By comparison with first column, second and third columns show a result of different metallic objects. Fourth, fifth and sixth columns show a result of variations of metal geometries with different tissue backgrounds. The results show improvements for different metallic object (titanium) as well as iron. However the trained network does not perform well in terms of very highly-attenuating metallic object (gold). The mismatch metric d_{α}^{MA} was computed with $\alpha = 0.5$. ($C = 250$ HU/W=2500 HU.)

By subtracting the metal-induced inconsistent data from input sinogram, we generate corrected sinogram data (See Fig. 2). The proposed method made the training more effective by reducing a complexity of input data. Furthermore, the labeled data acquisition was relatively easy, because the network required ex-vivo metal sinogram data instead of in-vivo metal sinogram data. For the test images, we generated CT images containing simulated metallic inserts (iron, titanium, gold).

Fig. 5 shows the numerical simulation results for the proposed method. The first, second, third and fourth rows show the reference, uncorrected image, corrected image and the plot of Υ , respectively. Although the network was trained only one kind of metallic object (iron), the result shows improvements for different metallic object (titanium) as well as iron. The beam-hardening artifacts are substantially reduced in the corrected image. Moreover, morphological structure corrupted by beam-hardening effects is considerably recovered. However, some new streaking artifacts are produced along the boundary of metal. In order to compare the quantitative errors in the corrected image with the reference image, we computed the normalized root mean square difference (NRMSD) [16] on the outside of metal. The NRMSD (%) for each result is listed in Table I. The corrected image has the lower NRMSD than

TABLE I
NRMSD AND THE MISMATCH METRIC d_{α}^{MA}

Phantom	Uncorrected		Corrected	
	NRMSD(%)	d_{α}^{MA}	NRMSD(%)	d_{α}^{MA}
Pelvis 1	59.27	28.9444	21.52	0.8272
Pelvis 2	43.79	14.0458	19.62	0.3301
Pelvis 3	98.94	384.9466	83.55	67.5396
Pelvis 4	52.79	21.9255	17.27	1.0847
Pelvis 5	56.85	19.3657	29.92	5.1090
Pelvis 6	49.42	16.5677	23.90	2.3481

uncorrected image. In terms of the mismatch metric d_{α}^{MA} , the results show that the mismatch of corrected sinogram was reduced.

IV. DISCUSSION AND CONCLUSION

This paper presents a deep learning method for MAR. Conventional methods for MAR are based on regularizations, and have the fundamental drawback of being not easily able to use manifold CT images, while a deep learning approach has the potential to do so. The fundamental challenge is to

collect enough labeled training data, a necessary step for a deep learning process. We circumvent this issue simply by using simulated training data as the basis for learning sinogram repair. We use the fact that the geometry of a metal trace region in a sinogram is non-linearly related to the beam-hardening feature. We use a U-net to learn the map from the geometry of the metal trace region to the corresponding beam-hardening factor. Results demonstrate that the proposed method can effectively remove metal-induced inconsistencies.

Deep learning methods are empirical, and lack rigorous theoretical grounding. Their outputs thus might be undesirable for medical diagnosis. Therefore, to assess the quality of the output, an acceptance check is developed that evaluates the extent and characteristics of artifacts induced by highly attenuating materials from sinogram data. The proposed metric can evaluate metal artifacts as shading or streaking artifacts. Numerical simulations and phantom experiments show that it effectively estimates both types in a quantitative manner. Let us briefly discuss conventional regularization techniques such as compressed sensing using ℓ_1 -regularization. These approaches can effectively prevent inadmissible solutions, but they discard detailed information (e.g., they remove small anomalies containing clinically useful information for diagnosis), and hence they have limited applicability to computed medical imaging. Deep learning has the potential to learn non-linear regression for various artifact sources, because it effectively uses complicated prior knowledge of CT images and artifacts.

There is much room for improvement, and further research is necessary to deal with various metal and bone-related artifacts. This paper does not consider artifacts that arise from nonlinear partial volume effects or electric noise, and the proposed metric requires the proper choice of weighting parameter for clinical use, so that streaking and shading artifacts are evaluated in an effective manner. Our future research will involve further investigation of this parameter.

ACKNOWLEDGEMENTS

The authors (S. M. Lee, H. P. Kim, and J. K. Seo) was supported by Samsung Science & Technology Foundation (No. SSTF-BA1402-01). The first author (H. S. Park) was partially supported by the National Research Foundation of Korea(NRF) grant funded by the Korea government(Ministry of Science, ICT & Future Planning) (No. NRF-2016R1C1B2008098) and the National Institute for Mathematical Sciences (NIMS) grant funded by the Korean government (No. A21300000).

REFERENCES

- [1] Barrett J F and Keat N 2004 Artifacts in ct: recognition and avoidance *Radiographics* **24** 1679–91
- [2] Bracewell R N and Riddle A C 1967 Inversion of fan-beam scans in radio astronomy *Astron. J.* **150** 427
- [3] Buls N, *et al* 2015 Contrast agent and radiation dose reduction in abdominal CT by a combination of low tube voltage and advanced image reconstruction algorithms *Eur. radiol.* **25** 1023–31
- [4] Bushberg J, Seibert J, Leidholdt Jr E and Boone J 2002 *The Essential Physics of Medical Imaging* (Philadelphia: Lippincott Williams & Wilkins)
- [5] Esberger U, *et al* 2013 CT evaluation of coronary artery stents with iterative image reconstruction: improvements in image quality and potential for radiation dose reduction *Eur. Radiol.* **23** 125–32
- [6] Garcia D 2010 Robust smoothing of gridded data in one and higher dimensions with missing values, *Comput. Stat. Data. An.* **54** 1167–78
- [7] Herman G T and Trivedi S S 1983 A comparative study of two postreconstruction beam-hardening correction methods *IEEE Trans. Med. Imag.* **2** 128–35
- [8] Hsieh J 1998 Adaptive streak artifact reduction in computed tomography resulting from excessive X-ray photon noise *Med. Phys.* **25** 2139–47
- [9] Hubbell J H and Seltzer S M 1996 Tables of X-ray mass attenuation coefficients and mass energy-absorption coefficients, *National Institute of Standards and Technology*
- [10] Poludniowski G, Landry G, DeBlois F, Evans P M and Verhaegen F 2009 Spekcalc: a program to calculate photon spectra from tungsten anode x-ray tubes *Phys. Med. Biol.* **54** N433
- [11] Ronneberger O, Fischer P, and Brox T 2015 U-net: Convolutional networks for biomedical image segmentation, In International Conference on Medical Image Computing and Computer-Assisted Intervention, pp. 234–241, Springer.
- [12] Beer A 1852 Bestimmung der absorption des rothen lichts in farbigen flüssigkeiten *Annalen der Physik* **162** 78–88
- [13] Lambert J H and Anding E 1892 Lamberts Photometrie: Photometria, Sive De Mensura et Gradibus Luminis, Colorum et Umbræ no. V. 1–2, Ostwalds Klassiker der exakten Wissenschaften
- [14] Tieleman T and Hinton G, 2012 Lecture 6.5-rmsprop: Divide the gradient by a running average of its recent magnitude, COURSERA:Neural Networks for Machine Learning.
- [15] Google 2015 TensorFlow: Large-scale machine learning on heterogeneous systems, URL <http://tensorflow.org/>. Software available from tensorflow.org.
- [16] Mehranian A, Ay M R, Rahmim A and Zaidi H 2013 X-ray CT metal artifact reduction using wavelet domain sparse regularization, *IEEE Transactions on Medical Imaging*. **32** 1702–1722